Article

Low-Temperature Nitrogen Doping of Nanocrystalline Graphene Films with Tunable Pyridinic-N and Pyrrolic-N by Cold-Wall Plasma-Assisted Chemical Vapor Deposition

Nur Hamizah Zainal Ariffin, Muhammad Aniq Shazni Mohammad Haniff,* Mohd Ismahadi Syono, Mohd Ambri Mohamed, Azrul Azlan Hamzah, and Abdul Manaf Hashim*

Read Online

ACCESS | Metrics & More | Article Recommendations | SI Supporting Information

ABSTRACT: We report a viable method to produce nanocrystalline graphene films on polycrystalline nickel (Ni) with enhanced N doping at low temperatures by a cold-wall plasma-assisted chemical vapor deposition (CVD) method. The growth of nanocrystalline graphene films was carried out in a benzene/ammonia/argon ($C_6H_6/NH_3/Ar$) system, in which the temperature of the substrate heated by Joule heating can be further lowered to 100 °C to achieve a low sheet resistance of 3.3 kΩ sq^{-1} at a high optical transmittance of 97.2%. The morphological, structural, and electrical properties and the chemical compositions of the obtained N-doped nanocrystalline graphene films can be tailored by controlling the growth parameters. An increase in the concentration of atomic N from 1.42 to 11.28 atomic percent (at.%) is expected due to the synergetic effects of a high NH_3/Ar ratio and plasma power. The possible growth mechanism of nanocrystalline graphene films is also discussed to understand the basic chemical reactions that occur at such low temperatures with the presence of plasma as well as the formation of pyridinic-N- and pyrrolic-N-dominated nanocrystalline graphene. The realization of nanocrystalline graphene films with enhanced N doping at 100 °C may open great potential in developing future transparent nanodevices.
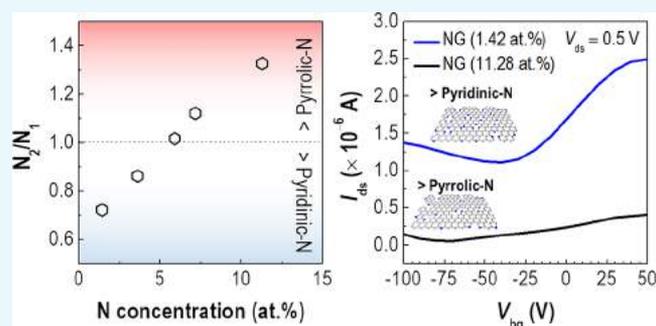
1. INTRODUCTION

Graphene, a two-dimensional material with sp²-hybridized carbon atoms arranged in a honeycomb lattice, has gained great attention from researchers for its unique properties in terms of optical, electronic, mechanical, and chemical properties.[1] In view of these, it has been considered as one of the promising materials for widespread applications such as field-effect transistors,[2] transparent conductive films,[3,4] solar cells,[5] photodetectors,[6−8] sensors,[9−11] and so forth. However, the utilization of graphene in most nanoelectronic applications is restricted due to its gapless states in pristine form.[12,13] To exploit possible modifications or tailoring its properties, it is, therefore, necessary to control the charge carrier concentration by tuning the Fermi level (E_F). The method applied for band gap tuning in graphene is through doping such as surface transfer doping, substitutional doping, or chemical doping.[14]

Substitutional doping of heteroatoms such as boron (B) or nitrogen (N) in the graphene is one of the most investigated methods since it is inherently stable due to the covalent bond linkage of the dopant into the graphene lattice.[15] Among B and N atoms, N substitution in graphene is most preferable due to its excellent properties such as comparable atomic size and possession of five valence electrons.[16] Particularly, N-doped graphene has three common bonding configurations known as

pyrrolic-N, pyridinic-N, and graphitic-N. Pyridinic-N refers to a N atom that substitutes within the two carbon (C) atoms at the edges or defects of graphene and contributes one *p* electron to the π system, while pyrrolic-N refers to a N atom that substitutes into the five-membered ring and contributes two *p* electrons to the π system. However, graphitic-N refers to a N atom that substitutes for C atoms in the hexagonal rings.[17] For instance, these bonding configurations have a significant effect on the charge distribution of the carbon network and may work as activation sites on the graphene surface, i.e., pyridinic-N is believed to be associated with oxygen reduction reaction (ORR) activities due to the availability of a single lone pair of the electron, which is considered as an active catalytic center.[18]

Direct synthesis through the chemical vapor deposition (CVD) method is widely used to produce N-doped graphene
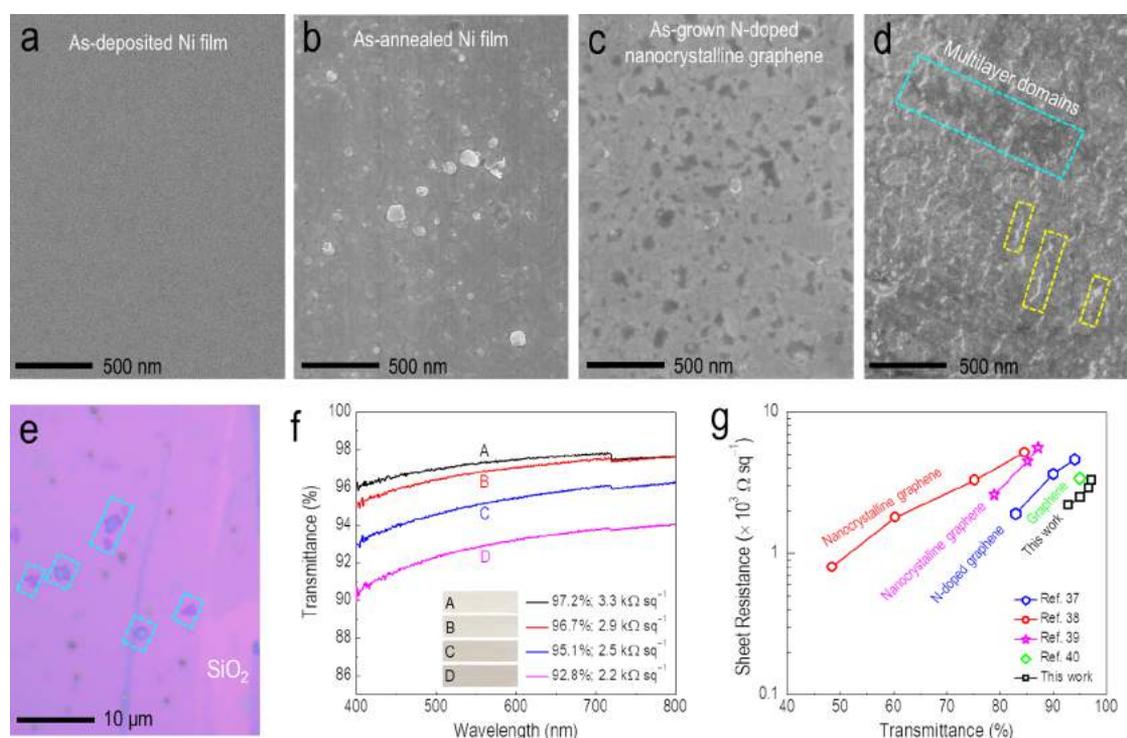
Figure 1. Morphological and electrical properties of N-doped nanocrystalline graphene films. FESEM images of (a) as-deposited Ni film, (b) as-annealed Ni film, (c) as-grown N-doped nanocrystalline graphene films on the Ni film, and (d) as-transferred N-doped nanocrystalline graphene films on the $SiO_2/Si(100)$ substrate The SiO_2 surface can be seen in the yellow box. (e) Optical micrograph of N-doped nanocrystalline graphene films on $SiO_2/Si(100)$ substrate showing several spots of multilayer domains underneath the top layers in the cyan box. The SiO_2 surface is represented by light color contrast. (f) Optical transmittance of N-doped nanocrystalline graphene films at different growth conditions. The insets show the photographs of N-doped nanocrystalline graphene samples transferred onto the quartz substrate on white paper background. (g) Comparison of the sheet resistance and optical transmittance obtained in the present work and other existing works in the literature.

because of its economic efficiency, scalability, and acceptance by the semiconductor industry. A typical CVD route to produce N-doped graphene has been reported using various carbon precursors such as methane, acetylene, or pyridine at high temperatures in the range of 800−1050 °C.[19−22] In most cases, high-temperature processes mostly result in dominant graphitic-N configuration over the large-area graphene.[19,23] Great deal of effort is always required in limiting the high-temperature processes due to severe physical damage to the substrates or devices, especially during the integration of graphene onto the nanoelectronics platform. Therefore, low-temperature growth of graphene is highly desirable as it is a more economical and convenient process on any low-temperature substrate. To achieve this, Ni and alloy metals have been reported as suitable catalysts for further reduction of the growth temperature while maintaining the same graphene quality as compared to that obtained by high-temperature processes.[24,25]

On the other hand, one promising way to realize the low-temperature growth of N-doped graphene is employing plasma-assisted CVD.[26−30] It is believed that the plasma does not only further lower the temperature for the growth of N-doped graphene but also can provide substantial free radicals for highly efficient N substitution in the direct growth of nanographene films. Meanwhile, several groups have demonstrated that the reduction of the growth temperature can be achieved using polyhalogenated aromatic compound[26] or heteroatoms containing carbon sources such as pyridine[31,32] that possess a similar structure to benzene for producing high-quality graphene.[33] A few studies have also been demonstrated

that the growth temperature of N-doped graphene can be lowered to 435 °C, in which the N atoms are mainly incorporated in the pyridinic-N form.[28,29] Meanwhile, at a much lower temperature of 300 °C, a recent study of N-doped graphene grown on Cu foils using liquid pyridine via two-step CVD demonstrated high-quality graphene films with dominant graphitic-N, but the N atomic concentration was low at around 1.6 at.%.[32] Although the growth of N-doped graphene has been reported previously, none of the systematic studies were focused on achieving nanographene films with high N doping concentration at low temperatures, particularly below 200 °C for cost-effective advanced electronic and electrochemical applications such as sensors and fuel cells.[34]

In this study, we report a viable method to extend the growth capabilities of N-doped nanocrystalline graphene films with enhanced N doping at low temperatures as low as 100 °C using a cold-wall plasma-assisted CVD system. This is the lowest temperature that has been reported to date for the growth of N-doped nanocrystalline graphene. In this method, we combine Joule heating and the plasma-assisted growth process at low-temperature regimes and use a $C_6H_6/NH_3/Ar$ system to produce large-area N-doped nanocrystalline graphene films on a polycrystalline Ni catalyst in a shorter time as compared to the existing hot-wall CVD method. The influences of the NH_3/Ar ratio and plasma power on the morphological, chemical composition, structural, and electrical properties of N-doped nanocrystalline graphene films are systematically studied. The findings suggest that the strong synergetic effects of the NH_3/Ar ratio and plasma power are key to this synthesis route and offer fine-tuning control over
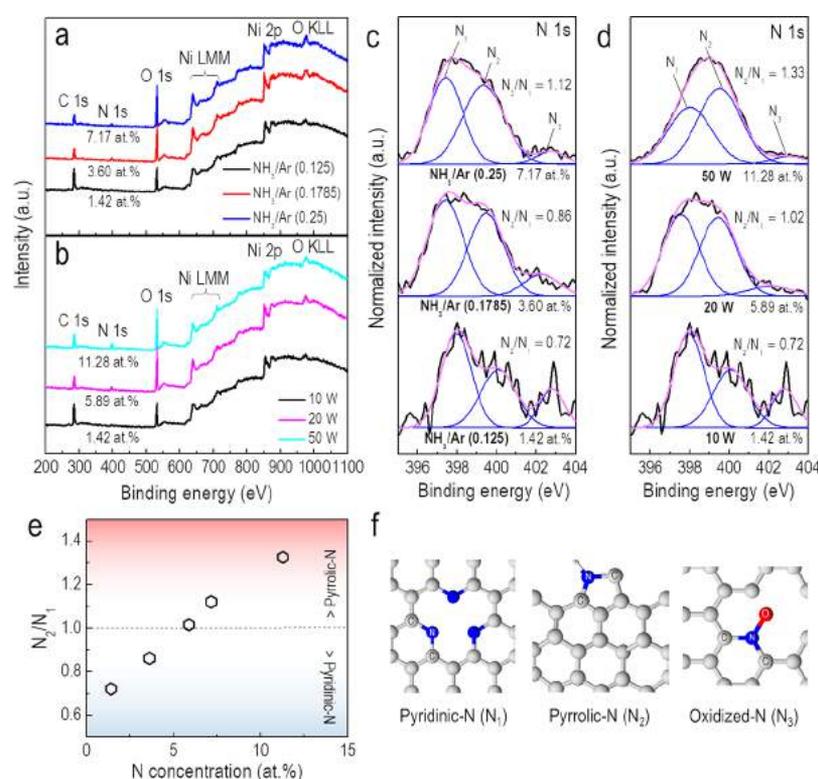
Figure 2. X-ray photoelectron spectroscopy (XPS) spectra of N-doped nanocrystalline graphene films. (a) XPS survey spectra of as-grown samples by varying the NH_3/Ar ratio at 0.125, 0.1785, and 0.25. (b) XPS survey spectra of as-grown samples by varying RF plasma power at 10, 20, and 50 W. (c, d) Corresponding core-level of N 1s spectra. (e) Ratio of pyrrolic-N to pyridinic-N content (N_2/N_1) as a function of atomic N concentration. (f) Schematic representation of possible nitrogen bonding configurations. N_1, N_2, and N_3 denote pyridinic-N, pyrrolic-N, and oxidized N, respectively.

macroscopic features to enable substantial N doping into the graphene lattice. The possible growth mechanism with pyridinic-N- and pyrrolic-N-dominated nanocrystalline graphene at low-temperature regimes is also discussed to demonstrate the tunability of N doping concentration.

2. RESULTS AND DISCUSSION

A field-emission scanning electron microscopy (FESEM) system was used to characterize the surface morphologies of the N-doped nanocrystalline graphene films before and after the growth process. The as-deposited 150 nm thick Ni on a $SiO_2/Si(100)$ substrate at room temperature, as shown in Figure 1a, exhibited a continuous film with ultrafine grain size (<10 nm). After annealing at an elevated temperature of up to 700 °C in H_2 for 30 min, significant grain growth and densification of Ni film were achieved on the surface of the substrate due to the variation of compressive thermal mismatch coefficient between the Ni film and SiO_2/Si substrate.[35] The as-annealed Ni film has an average grain size of about 250 nm, and the grains were densely packed without any carbonaceous growth on the Ni surface (see Figure 1b). This was confirmed by Raman spectrum analysis, in which no G, D, and 2D bands were seen for the samples before and after the annealing process in H_2/Ar (see Figure S1). In this case, the results suggest that no graphene or amorphous carbon formation was taken place on the Ni surface during the annealing step. After the growth process in $C_6H_6/NH_3/Ar$ plasma, the grain size of the Ni film remains unchanged at all. The visibility of color contrast (light and dark region) indicates the formation of nanocrystalline

graphene films on the Ni grains and $SiO_2/Si(100)$ substrate (see Figure 1c,d). Both lighter and darker regions are representative of thin and thick layers, as commonly reported previously.[36] It is expected that the high nucleation density and high growth rate of plasma-assisted CVD may cause stacking of graphene in few-layer or multilayer domains, which can be clearly seen in an optical image of the transferred sample (see Figure 1e). Most importantly, the morphology of N-doped nanocrystalline graphene in this work resembles a layer of continuous films on the $SiO_2/Si(100)$ substrate.

Additional characterization by the visible spectroscopy system has been performed to measure the optical transmittance of N-doped nanocrystalline graphene samples. As reported, light transmittance could identify the number of graphene layers on the quartz substrate, where the wavelength value is commonly taken in the visible range starting from 400 to 800 nm under incident white light.[36] Prior to characterization, the as-grown N-doped nanocrystalline graphene films were carefully transferred onto a quartz substrate using the typical wet chemical transfer technique. As shown in Figure 1f, the optical transmittance of N-doped nanocrystalline graphene films exhibits a highly transparent film all over the visible range, in which the values of optical transmittance decrease with increasing growth temperature. The sample grown at 100 °C exhibits optical transmittance of 97.2% at 550 nm and 97.8% at 700 nm. The high values of optical transmittance in this work are slightly lower compared to that of the typical monolayer graphene (97.7%) reported previously.[36] The slight variation is possibly attributed to the poor coverage of graphene in the form of bilayer or multilayer domains. In addition, the

Table 1. Direct Growth of the N-Doped Graphene CVD Method from This Present Work and Other Existing Works

precursors	pressure (Pa)	catalyst	temperature (°C)	nitrogen content (at.%)	main configuration	ref
methane/ammonia (CH_4/NH_3)	atm	Cu film	800	1.2–8.9	graphitic-N	19
ethylene/ammonia (C_2H_4/NH_3)	613	Cu foil	900	0–16	pyridinic-N	20
pyridine (C_6H_6N)	933.3	Cu foil	1000	2.4	pyridinic-N	22
poly(dimethylsiloxane)/hydrogen/nitrogen ((C_2H_6OSi)$_n$/H_2/N_2)	3066.4	Cu foil	700	0.9–5.6	pyrrolic-N	27
1,3,5-triazine (HCN)$_3$	666.6	Cu foil	700–900	2.1–5.6	pyridinic-N/pyrrolic-N	42
pyridine (C_6H_6N)	0.133	Cu foil	950	0.18	graphitic-N	23
pentachloropyridine (C_5Cl_5N)	2000	Cu foil	400–600	1.7–8.2	pyrrolic-N	44
			200–300	7.3–8.5	graphitic-N	
pyridine (C_6H_6N)	atm	Cu foil	300	1.6	graphitic-N	32
benzene/ammonia/argon ($C_6H_6/NH_3/Ar$)	200	Ni film	100	1.42–3.60	pyridinic-N	present work
				5.89–11.28	pyrrolic-N	

transparency and visual homogeneity of the N-doped nanocrystalline graphene films are also shown in the inset of Figure 1f. For electrical measurements, the as-transferred N-doped nanocrystalline graphene films (1.0 cm × 1.0 cm size) on the quartz substrate were characterized using a typical van der Pauw method under ambient air at 300 K by a Hall-effect measurement system. At a high optical transmittance value of 97.2%, the extracted average sheet resistance (R_s), sheet concentration (n), Hall mobility ($|\mu_{Hall}|$), and Hall effect coefficient ($|R_{Hall}|$) of the N-doped nanocrystalline graphene films were determined to be 3.3 kΩ sq^{-1}, 7.51 × 10^{13} cm^{-2}, 65.5 cm^2 V^{-1} s^{-1}, and 5.41 cm^3 C^{-1}, respectively. For comparison with existing plasma-assisted CVD, a plot of sheet resistance versus optical transmittance is shown in Figure 1g. The average sheet resistance of N-doped nanocrystalline graphene films in this work is almost comparable to that of nanocrystalline graphene films grown at much higher temperature regimes.[37−40]

X-ray photoelectron spectroscopy (XPS) is the standard characterization technique to study the nitrogen doping phenomenon. To examine the concentration of atomic N in the N-doped nanocrystalline graphene films, XPS survey spectra were first measured by scanning the as-grown samples at the lowest growth temperature of 100 °C with different NH_3/Ar ratios, as shown in Figure 2a,b. The results of the XPS survey scans for all N-doped nanocrystalline graphene films show typical three C 1s, N 1s, and O 1s peaks at ∼284.8, ∼399.1, and ∼531.2 eV binding energies, respectively. It was observed that the intensity of the C 1s peak is much lower at a higher NH_3/Ar ratio and plasma power, while the intensities of other peaks exhibit an opposite trend. Here, the presence of a minor N 1s peak can be attributed to the C−N bonds in the graphene lattice, which is consistent with our previously reported N-doped graphene.[41] Using a constant RF power of 10 W, the concentration of atomic N tends to monotonically increase with an increase in the NH_3/Ar ratio as a result of the high precipitation of NH_3 during the growth process. The concentration of atomic N shows an increasing trend with the values of 1.42, 3.60, and 7.17 at.% for the 0.125, 0.1875, and 0.25 of NH_3/Ar ratios, respectively. Similarly, the concentration of atomic N also tends to increase with an increase in plasma power. The values of the concentration of atomic N are determined to be 1.42, 5.89, and 11.28 at.% at 10, 20, and 50 W RF plasma power, respectively. Here, the enhanced N doping up to 11.28 at.% is the highest reported N doping concentration to date for the direct growth CVD process,

implying the role of plasma in enabling substantial N doping at a growth temperature of 100 °C. It is also noted that the N-doped graphene films have a higher N doping concentration at lower growth temperatures.[21,42,43] For comparison, the results for the present and previous N-doped graphene are summarized in Table 1. In this method, the results suggest that a high N doping concentration is possible to achieve for the growth of N-doped nanocrystalline graphene films at temperatures as low as 100 °C. To confirm the distribution of elemental composition in N-doped nanocrystalline graphene, energy-dispersive X-ray spectroscopy (EDS) elemental mapping analysis was carried out on a mapping area of 18.5 μm × 25 μm. The EDS results show that the samples grown on the Ni film at 10, 20, and 50 W RF power consist of the typical C, O, and N elements, which are distributed uniformly on the top surface (see Figure S2). The N/C atomic ratios for the samples grown on the Ni film at 10, 20, and 50 W are determined to be 0.072, 0.094, and 0.237, respectively. Here, the increase in the N/C atomic ratio obtained in this work indicates substantial N doping in the graphene lattice plane.

To further investigate the possible N bonding configuration in the N-doped nanocrystalline films, the high-resolution XPS scans of N 1s were carefully carried out at several scan spots of the as-grown samples. After applying the Shirley background subtraction, a Gaussian−Lorentzian product function was used to approximate the line shapes of the fitting components. Figure 2c,d shows the deconvolution of core-level N 1s spectra of N-doped nanocrystalline graphene films with different NH_3/Ar ratios and plasma power levels. There are three components obtained for the core-level N 1s spectra at ∼397.5−398.1, ∼399.4−400.1, and ∼402.2−402.9 eV, which correspond to pyridinic-N (N_1), pyrrolic-N (N_2), and oxidized N (N_3), respectively (see Figure 2f). Here, no significant peak can be seen at ∼401 eV, which corresponds to graphitic-N for all of the as-grown samples, indicating that pyridinic-N and pyrrolic-N are both preferred to bond with C atoms over graphitic-N. At a relatively low temperature of 100 °C, none of the N atoms is expected to substitute a C atom and bonding with three C atoms directly in hexagonal lattice structure at the basal plane. Based on the results of core-level N 1s spectra, it is suggested that the changes of the N bonding configuration in the N-doped nanocrystalline graphene films are dependent on the growth parameters. At a constant 10 W RF power, the growth of N-doped nanocrystalline graphene films with 0.125 NH_3/Ar ratio tends to adopt more pyridinic-N over pyrrolic-N and oxidized N configuration, especially at the edges or defects.
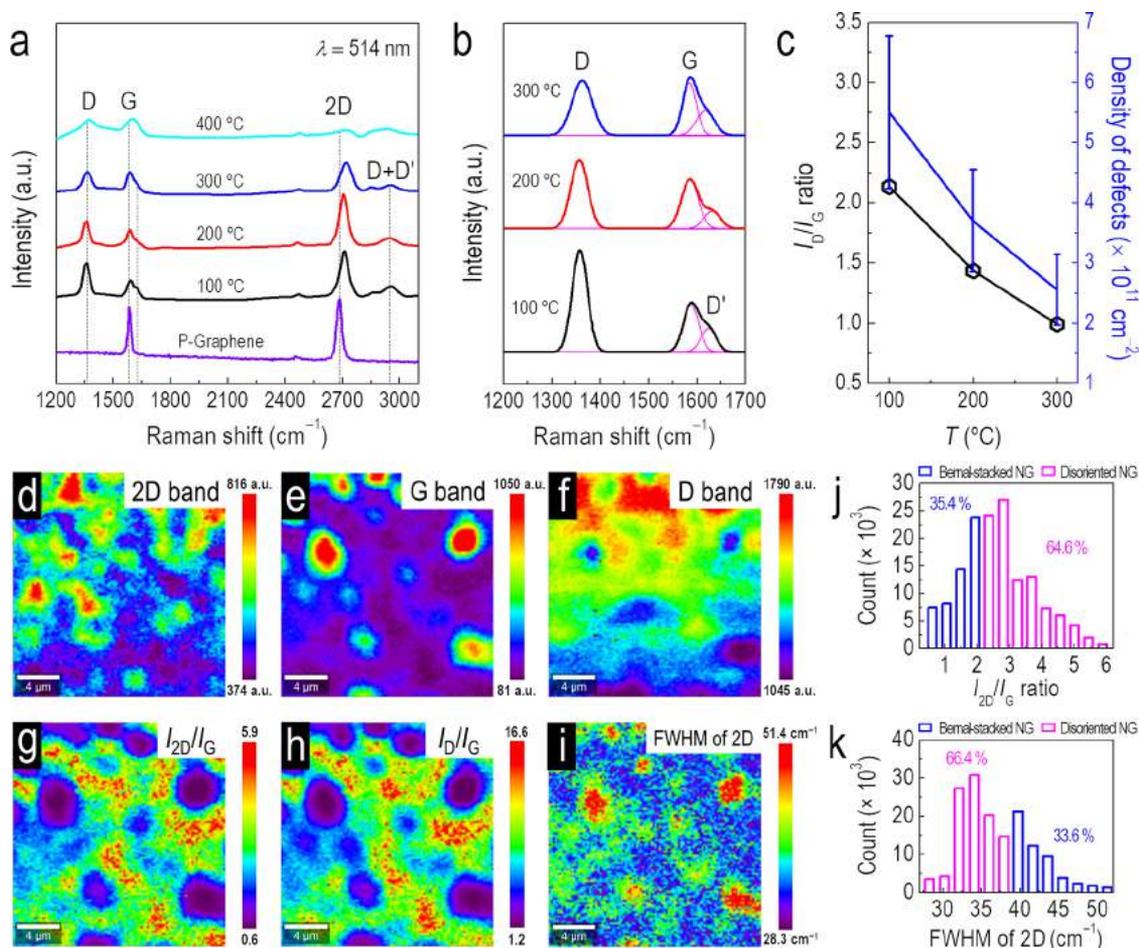
Figure 3. Raman spectra measurements of N-doped nanocrystalline graphene films grown at low-temperature regimes. (a) Raman spectra of N-doped nanocrystalline graphene films transferred on the $SiO_2/Si(100)$ substrate at different growth conditions. (b) Deconvoluted profile of the D, G, and D′ bands in (a) after baseline correction. (c) Peak intensity ratio of the D band to G band (I_D/I_G) and the density of defects (n_D) as a function of growth temperature (T). (d−i) Raman map intensities of the 2D band, G band, D band, I_{2D}/I_G, I_D/I_G, and FWHM of the 2D band. The mapping area of the N-doped nanocrystalline graphene films is 20 μm × 20 μm. (j, k) Histogram plots of the peak intensity ratio of the 2D band to G band (I_{2D}/I_G) and the full width at half-maximum (FWHM) of the 2D band indicating the distribution areas of Bernal-stacked and disoriented nanographene (NG) domains.

When the NH_3/Ar ratio is increased from 0.125 to 0.25, pyrrolic-N tends to be a more dominant configuration compared to others, in which the ratio of pyrrolic-N to pyridinic-N (N_2/N_1) content increases from 0.72 to 1.12. A similar trend of increasing pyrrolic-N is also observed when the RF power is increased from 10 to 50 W, in which the N_2/N_1 increases from 0.72 to 1.33. Meanwhile, less oxidized N is observed at a higher NH_3/Ar ratio and plasma power because this configuration is likely to break from the graphene lattice, and eventually form volatile molecules upon breaking. Based on the values of N_2/N_1 in Figure 2e, the N doping with more pyrrolic-N than pyridinic-N ($N_2/N_1 > 1$) can be achieved especially at a higher N doping concentration (≥5.89 at.%) and vice versa. The findings suggest that pyridinic-N- and pyrrolic-N-dominated nanocrystalline graphene can be specifically tuned by controlling the NH_3/Ar ratio and plasma power during the growth process.

Based on the above observations, a possible growth mechanism for the dominant pyridinic-N or pyrrolic-N in the graphene lattice based on XPS results is proposed to understand the growth of N-doped nanocrystalline graphene via plasma-assisted CVD. First, it should be noted that the source of dehydrogenation of C_6H_6 in this study consists of two parts: plasma and Ni catalyst. Upon introducing the gas mixture of $C_6H_6/NH_3/Ar$ into the reaction chamber at 100 °C, the uniform plasma generated by two parallel plates (e.g., gas showerhead and heater stage) on the Ni surface continuously dissociates $C_6H_6-NH_3$ molecules into highly reactive C_xH_y species (radicals, ions) ($x < 6$, $y < 6$), NH_y species ($y < 3$) and generates reactive H species in a controlled manner. Through this process, the H species may contribute to further dissociation of the $C_6H_6-NH_3$ molecules and introduce H_2 during the plasma-assisted process.[45] In addition, the H and Ar species also remove impurities and amorphous carbon generated on edges and thus keep the edges active during the nucleation and expansion process.[46] Although the C_6H_6 molecules can be thermally dehydrogenated at low-temperature regimes, the dehydrogenation of C_6H_6 molecules partially takes place,[47] and thus incorporating NH_3 molecules is necessary to enhance the efficiency during the plasma-enhanced dissociation reactions.[26,48] In particular, H species from the dissociation of the NH_3 molecules are likely to hydrogenate with H species from the dissociated C_xH_y species and introduce additional H_2; thus, the dehydrogenation efficiency of C_6H_6 increases. Possible chemical interaction to produce N-doped nanocrystalline graphene can be expressed

by the following equilibrium: C_6H_6 (g) + 2NH$_3$ (g) + Ar (g) ⇌ N-doped graphene (s) + 6H$_2$ (g) + Ar (g) − Q, in which Q is the heat. At a low NH$_3$/Ar ratio or low plasma power, fewer H species are likely to initiate the nucleation of small graphitic clusters from the assembly of C_6 rings on the Ni surface and result in high coverage of the nanocrystalline graphene film on the Ni surface. In parallel, more C_xH_y species in the form of C_6 rings are generated to form covalent bonds with NH$_y$ species at the edges and graphitic basal plane during the adsorption of C_xH_y−NH$_y$ species on the Ni surface, hence resulting in more pyridinic-N (sp^2-coordinated, two N−C bonds in a hexagon) than pyrrolic-N (sp^3-coordinated, two N−C bonds in a pentagon). This behavior is contrary to the early attempts of low-temperature graphene growth that suffer from low surface coverage and in the form of flakes rather than as a film.[31] In contrast, at a high NH$_3$/Ar ratio or high plasma power, the densities of C_6H_6 and NH$_3$ molecules tend to increase more intensely and more H species are generated during the C_6H_6−NH$_3$ dissociation reactions probably lead to significant edge etching. NH$_y$ species tend to attach to the edges and form NH-terminated edges to increase the energy barrier for C species attachment. On the other hand, some of the C_6H_6 molecules tend to partially dissociate into C radical fragments or broken graphitic sp^3 carbon instead of forming C_6 rings for the assembly of the nanocrystalline graphene layer. Therefore, strong interaction between the NH$_y$ species and the graphene edges is expected to take place, especially at the edges or defects, resulting in more pyrrolic-N than pyridinic-N due to the strong influence of reactive NH$_y$ species.

Raman spectroscopy is another useful tool to characterize the N-doped nanocrystalline graphene films. The influence of growth temperature on the structural properties of N-doped nanocrystalline graphene film was first investigated and compared with the pristine CVD graphene, as shown in Figure 3a. Raman spectra of pristine CVD graphene present typical intense Raman features: the G band at 1583 cm^{-1} and the 2D band at 2684 cm^{-1}. In addition to these two peaks, the N-doped nanocrystalline graphene film at lower growth temperature presents a D band of much stronger peak intensity located at 1357 cm^{-1}, which is activated by intervalley scattering, indicating the presence of higher defects or impurities from the substitution of N atoms into the graphene lattice. Meanwhile, at higher growth temperatures, the peak intensity of the 2D band in the N-doped nanocrystalline graphene film is much weaker compared to that in pristine graphene, which is consistent with the previously reported N-doped graphene.[49] However, the peak intensity of the 2D band almost deteriorates for the sample grown at 400 °C, which indicates the formation of amorphous carbon. This could be attributed to the higher electron−hole scattering rate from either the N-induced electron doping or lattice defects.[50] Additional weak D′ and D + D′ peaks located at 1624 and 2950 cm^{-1} are also noticeable for the samples grown at 100, 200, and 300 °C, which are activated by intravalley scattering and combination of phonons with different momenta around K and Γ points, respectively. Here, the D′ peak is merged into the G peak due to intrinsic defects in the nanocrystalline graphene films.[51] From deconvolution of Raman spectra, as shown in Figure 3b, a sharp G peak profile is expected for the as-grown samples that is distinct from those of amorphous carbon and diamondlike films grown by the plasma method.[52] In addition, the shift of Raman peaks can also provide doping information of the graphene lattice.[53] In comparison to the

pristine graphene, the G and 2D bands for the sample grown at 100 °C are shifted to the higher frequencies with an average blue shift of ∼3.4 and ∼18.7 cm^{-1}, respectively. Noted that the blue shift in the G band is due to the presence of pyridinic-N and pyrrolic-N, which is in accordance with reported N-doped graphene.[54] This means that our nanocrystalline graphene films are successfully doped by N atoms.

Generally, the peak intensity ratio of D band to G band (I_D/I_G) indicates the degree of defects in in-plane graphene,[55] which usually shows a strong dependence on the growth temperature. In this study, the mean values of the I_D/I_G ratio are expected to increase from 1.0 to 2.13 when decreasing the growth temperature from 300 to 100 °C (see Figure 3a). The mean values of I_D/I_G in this work are much higher than that of typical polycrystalline N-doped graphene (I_D/I_G = ∼0.3−0.4) produced by the high-temperature CVD method.[56] From the mean values of I_D/I_G, the density of defects of the N-doped nanocrystalline graphene can be evaluated using the following general equation:[55] $n_D = ((1.8 \pm 0.5) \times 10^{22}) \cdot \lambda^{-4} \cdot (I_D/I_G)$, where λ is the laser excitation wavelength used for the Raman measurements. Assuming that N doping is uniform in the graphene film, here, we estimate that the average defect densities of the N-doped nanocrystalline graphene are 5.49 × 10^{11}, 3.70 × 10^{11}, and 2.55 × 10^{11} cm^{-2} for the growth temperatures of 100, 200, and 300 °C, respectively (see Figure 3c). The high I_D/I_G in this work also reflects a common feature of polycrystalline nanodomains in the graphene grown using plasma. From the peak intensity ratio of the D band to G band, it is possible to estimate the graphitic domain size.[57] The domain size L_a can be estimated by the Tuinstra−Koenig relation $L_a = (2.4 \times 10^{-10}) \cdot \lambda^4 \cdot (I_D/I_G)^{-1}$. In particular, this yields an average domain size of 7.86 nm for the growth temperature of 100 °C, about 1 order of magnitude smaller than that of typical pristine graphene (>100 nm). This value indicates that the deposited graphene is not pure single-crystalline but nitrogen-containing polycrystalline graphene.

Next, Raman mapping measurements were also employed to further investigate the structural properties of the N-doped nanocrystalline graphene film at the lowest growth temperature of 100 °C. Large-area Raman mapping images of the as-grown sample within a 20 μm × 20 μm area were carefully obtained for the main 2D, G, and D bands, as shown in Figure 3d−f. Among these bands, the results of the D band at 1357 cm^{-1} show the highest values of intensity due to a high number of defects and high amount of N dopants in the graphene lattice, which is relatively consistent with the results of Raman spectra in Figure 3a. On the other hand, the results of the 2D band at 2703 cm^{-1} and the G band at 1587 cm^{-1} show fair values of intensity, indicating that the as-grown sample possesses high coverage of nanocrystalline graphene films over the large-area substrate. To examine the stacking order of nanocrystalline graphene films, further analysis of the Raman intensity map of I_{2D}/I_G and the full width at half-maximum (FWHM) of the 2D band was performed, as shown in Figure 3g,i. It is worth noting that the stacking order is determined based on the following I_{2D}/I_G and FWHM values of the 2D band: 0.6−2.0 (I_{2D}/I_G) and 41.0−51.4 cm^{-1} (FWHM of 2D) are for Bernal-stacked nanocrystalline graphene, whereas 2.1−5.9 (I_{2D}/I_G) and 28.3−40.5 cm^{-1} (FWHM of 2D) are for disoriented nanocrystalline graphene. Here, the distribution of the stacking order in nanocrystalline graphene is shown in the histogram plots of I_{2D}/I_G and FWHM of 2D (see Figure 3j,k), where both show comparable results. The disoriented nanocrystalline graphene
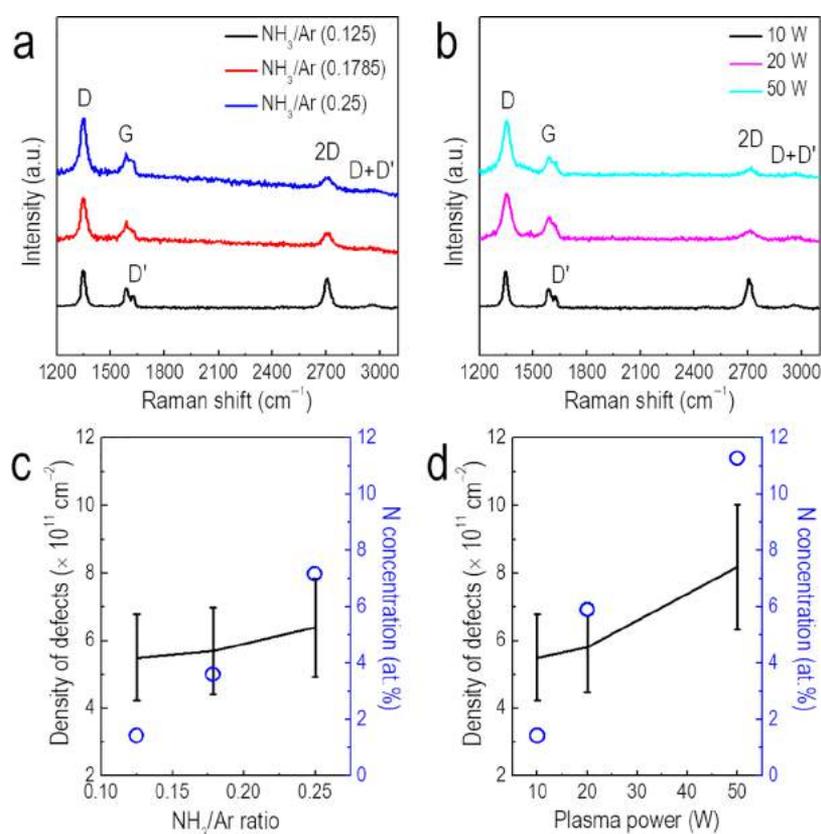
Figure 4. Raman spectra of N-doped nanocrystalline graphene films grown on the Ni film/SiO$_2$/Si(100) substrate with different (a) NH$_3$/Ar ratios and (b) plasma power levels. Density of defects and N doping concentration as a function of (c) NH$_3$/Ar ratio and (d) plasma power.
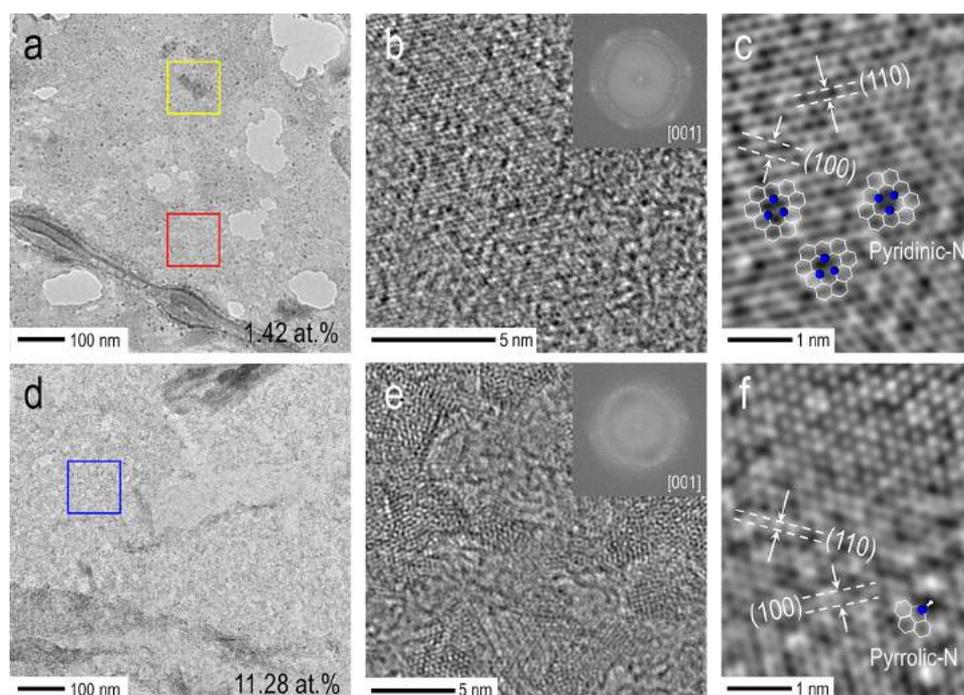

Figure 5. Characterization of the atomic structure of N-doped nanocrystalline graphene films grown at 100 °C. (a) TEM image of N-doped nanocrystalline graphene films with an atomic N doping concentration of 1.42 at.%. (b) HR-TEM imaging in a red square area in (a); the inset of (b) is the corresponding fast Fourier transform FFT pattern displaying the characteristic of the single-crystalline lattice structure. (c) Fourier filtered HR-TEM image showing the pyridinic-N configuration. (d) TEM image of N-doped nanocrystalline graphene films with an atomic N doping concentration of 11.28 at.%. (e) HR-TEM imaging in a blue square area in (d); the inset of (e) is the corresponding fast Fourier transform FFT pattern showing the typical Debye–Scherrer-type ring pattern. (f) Fourier filtered HR-TEM image showing the pyrrolic-N configuration.
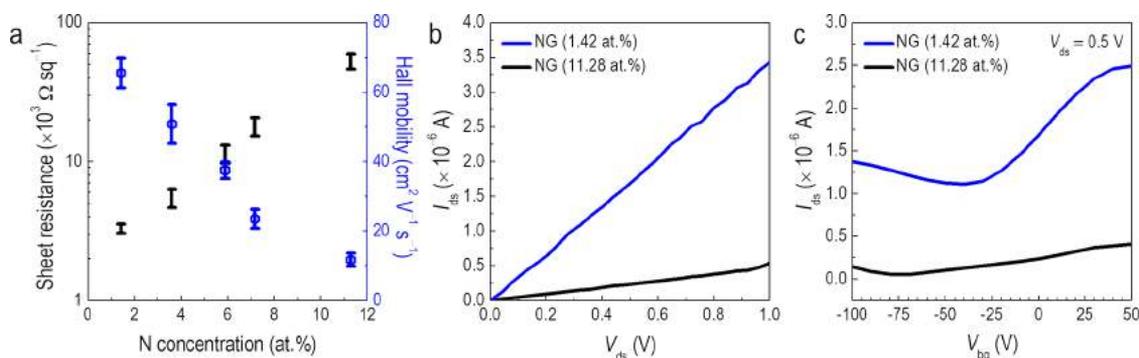
Figure 6. Electrical characterization of N-doped nanocrystalline graphene films. (a) Sheet resistance and Hall mobility as a function of the N doping concentration. (b) Source−drain current (I_{sd})−source−drain voltage (V_{sd}) characteristics at zero gate voltage (V_{bg}). (c) $I_{sd}−V_{bg}$ transfer characteristics at a constant V_{sd} of 0.5 V for the N-doped nanocrystalline graphene (NG) films with N doping concentrations of 1.42 and 11.28 at. %.

has relatively dominant coverage areas with 64.6−66.4%, while the remaining areas of 33.6−35.6% are covered by the Bernal-stacked nanocrystalline graphene. The observations also suggest that the highly disoriented nanocrystalline graphene region mostly correlates to a high number of defects, according to the Raman intensity map of I_D/I_G (see Figure 3h).

To confirm the tunability of the N doping concentration in N-doped nanocrystalline graphene, we used Raman measurements to correlate the defect density of the as-grown samples with the N doping concentration at different NH_3/Ar ratios and plasma power levels (refer to Figure 2a,b). Figure 4a,b shows the Raman spectra of the as-grown samples with different NH_3/Ar ratios and plasma power extracted from the Raman mapping measurements (see Figure S4). It was observed that the intensity of the D band increases, whereas the intensity of the 2D band decreases with increasing NH_3/Ar ratio and plasma power, suggesting substantial N doping accompanied by the appearance of structural defects. By varying the NH_3/Ar ratio, the I_D/I_G ratio shows an increasing trend with the mean values of 2.13, 2.21, and 2.48 for the 0.125, 0.1875, and 0.25 NH_3/Ar ratios, respectively. Also, an increase in plasma power may result in a drastic increase in the I_D/I_G ratio with the mean values of 2.13, 2.25, and 3.17 for the 10, 20, and 50 W RF plasma power levels, respectively. The density of defects (n_D) in relation to the N doping concentration is presented in Figure 4c,d. From the graphs, the estimated n_D of the N-doped nanocrystalline graphene is proportional to the NH_3/Ar ratio and plasma power, which correlates well with the increase in the N doping concentration as discussed previously.

The atomic structure of the N-doped nanocrystalline graphene film was characterized by high-resolution transmission electron microscopy (HR-TEM). Figure 5a,c displays the low-resolution bright-field TEM image of N-doped nanocrystalline graphene with N doping concentrations of 1.42 and 11.28 at.%, respectively. The N-doped nanocrystalline graphene at a low N doping concentration (1.42 at.%) transferred on a lacey carbon-coated Cu grid illustrates a few hundred square nanometer thin layer that is highly electron transparent in comparison to the lacey carbon support. Meanwhile, the one at a high N doping concentration (11.28 at.%) displays a destructive thin layer with more uneven features. The most transparent areas are likely identified as a thin layer of nanocrystalline graphene, whereas the dark areas indicate some structural folds and holes that were probably

formed due to improper handling of the sample during the wet chemical transfer process. Figure 5b shows the HR-TEM image of N-doped nanocrystalline graphene at a low N doping concentration (1.42 at.%) taken from the selected red square area in Figure 6a. Both HR-TEM and its corresponding fast Fourier transform (FFT) pattern show the single-crystalline nature of the graphitic domains in the hexagonal lattice form with some defects at the basal plane, which are quite similar to the reported N-doped graphene from previous works.[58,59] Conversely, the HR-TEM image of N-doped nanocrystalline graphene at a high N doping concentration (11.28 at.%) reveals small graphitic domains in a polycrystalline structure, which was further confirmed by the typical Debye−Scherrer-type ring pattern from the FFT pattern (see Figure 5e). From the HR-TEM analysis, the domain sizes of the N-doped nanocrystalline films with N doping concentrations of 1.42 and 11.28 at.% are estimated to be 5.22 ± 0.93 and 3.16 ± 0.88 nm, respectively.

To resolve an individual C atom in the hexagonal packing arrangement and provide the topography of an individual N dopant site, the HR-TEM image was carefully postprocessed by a typical Fourier mask filtering method.[60] From the images of Fourier filtered HR-TEM of the N-doped nanocrystalline graphene, as shown in Figure 5c,f, the atomic-scale measurements reveal lattice spacings of ∼0.25 and ∼0.14 nm corresponding to the (100) and (110) planes, respectively. In addition, the C atoms that are bonding with the N atom in the pyridinic-N and pyrrolic-N configurations within the graphene lattice are also observed, which correlate well with the XPS results in this study. The triangular dark spots surrounded by bright spots in graphene at the basal plane are assigned to the pyridinic-N configuration (see Figure 5c), whereas the dark spots associated with vacancy defects at the edges or defects are probably attributed to the incorporated N atoms corresponding to the pyrrolic-N configuration (see Figure 5f). Our observation here is quite similar to the previously reported graphene with pyridinic-N and pyrrolic-N.[61] Overall, even though the low-temperature growth was successfully demonstrated here, further optimizations of the growth parameters are still needed to achieve high-quality graphene films while maintaining substantial N doping in the graphene lattice plane. For example, the design of a high-quality single-crystalline catalyst would be a better route for the low-temperature plasma-assisted CVD methods in the near future.
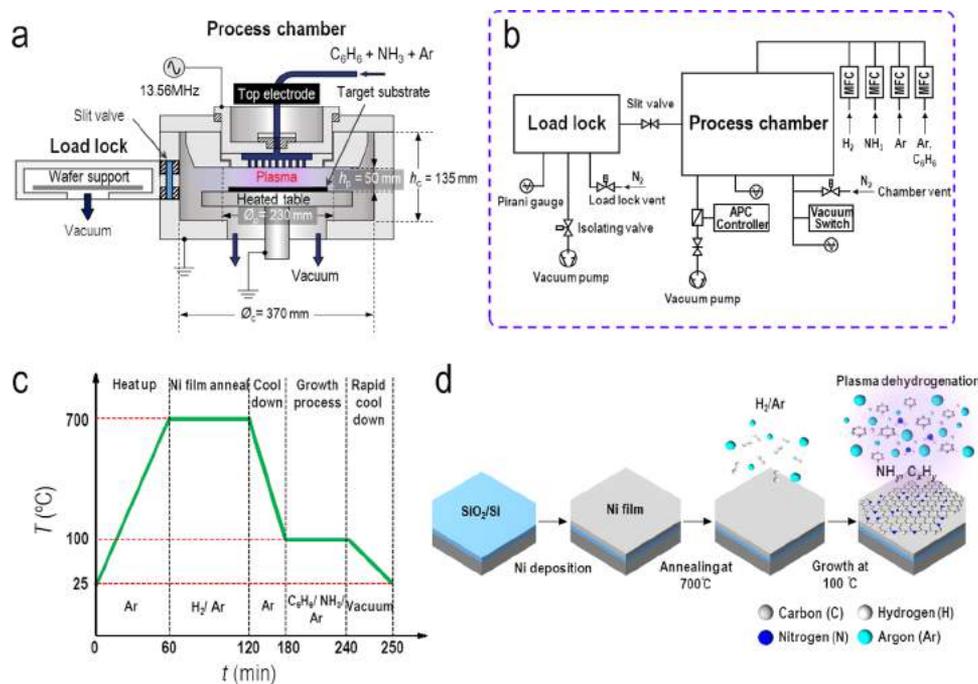
Figure 7. Experimental setup of low-temperature growth of N-doped nanocrystalline graphene films. (a) Schematic representation of the cold-wall plasma-assisted CVD method. (b) Layout of the vacuum system of the plasma-assisted CVD method. (c) Schematic diagram of the reaction temperature (T) versus duration (t) for the optimized growth parameters. (d) Schematic representation of the overall growth process of N-doped nanocrystalline graphene films.

Electrical measurements based on the van der Pauw method were first performed using a Hall-effect measurement system in ambient air at 300 K to evaluate the sheet resistance (R_s) and Hall mobility (μ_{Hall}) of N-doped nanocrystalline graphene films. The results of sheet resistance and Hall mobility as a function of the N doping concentration are shown in Figure 6a. It was revealed that the measured sheet resistance of N-doped nanocrystalline graphene films increases from 3.3 ± 0.3 to 52.8 ± 6.7 kΩ sq^{-1} with an increase in the N doping concentration. As a direct consequence of the increase in the sheet resistance, it was observed that the Hall mobility of the charge carriers decreases from 65.5 ± 4.4 to 11.7 ± 1.9 cm^2 V^{-1} s^{-1} with an increase in the N doping concentration. In this case, the Hall mobility mainly decreases due to the high scattering of defects and disorders in the graphene lattice, which is related to a high degree of N doping. Noted that the N-doped nanocrystalline graphene films dominated by pyridinic-N and pyrrolic-N are usually accompanied by the presence of defects that tend to localize the charge carrier transport. To further study the influence of N doping concentration on the electrical properties of N-doped nanocrystalline graphene films, a back-gated field-effect transistor (FET) using the N-doped nanocrystalline graphene films was fabricated by a standard photolithography process and characterized using a source meter unit (SMU) system (Keithley 236) in ambient air at 300 K. The FET structure consists of back gating of a p-type Si, 500 nm thick SiO$_2$ layer as gate oxidation, N-doped nanocrystalline graphene, and metal source and drain contacts (Au/Cr electrodes with 120/60 nm thickness). Figure 6b shows the typical source−drain current (I_{sd}) versus the source−drain voltage (V_{sd}) for the fabricated FET devices with the N-doped nanocrystalline graphene films at low (1.42 at.%) and high (11.28 at.%) N doping concentrations. Both devices exhibit a linear I_{sd}−V_{sd}

curve at zero gate voltage (V_{bg}) with low contact resistance, suggesting a good Ohmic contact between the N-doped nanocrystalline graphene films and the Au/Cr electrodes.

Figure 6c shows the source−drain current (I_{sd}) versus gate voltage (V_{bg}) at a constant V_{sd} of 0.5 V for the fabricated FET devices with the N-doped nanocrystalline graphene films at low (1.42 at.%) and high (11.28 at.%) N doping concentrations, at which the charge transport exhibits asymmetry in electron and hole conduction. It can be seen that I_{sd} increases with increasing positive gate bias for both devices, indicating an n-type semiconductor behavior.[32] In addition, the Dirac gate voltage was observed at −40 and −70 V for the devices with N doping concentrations at 1.42 and 11.28 at.%, respectively, suggesting the predominant electron transport in the N-doped nanocrystalline graphene films. Here, a clear trend toward a negative shift of the Dirac gate voltage (from −40 to −70 V) could be attributed to the increase in electron density distribution with increasing N doping concentration.[42] From the transfer characteristics of the devices, the electron and hole mobilities were extracted by estimating the linear region of I_{sd}−V_{bg} curves using equation[62] $\mu = (l/wC_{ox}V_{sd})/(\Delta I_{sd}/\Delta V_{bg})$, where l and w are the channel length (50 μm) and width (50 μm), respectively, and C_{ox} is the gate oxide capacitance per unit area (ca. 69.02 nF cm^{-2}) for the 500 nm thick SiO$_2$ layer. The electron and hole mobilities of the device at a low N doping of 1.42 at.% are 57.7 and 12.7 cm^2 V^{-1} s^{-1}, respectively. Meanwhile, at a high N doping of 11.28 at.%, the electron and hole mobilities of the device are 9.1 and 8.7 cm^2 V^{-1} s^{-1}, respectively. In this case, the electron and hole mobilities decrease upon a further increase in the N doping concentration and this finding is also consistent with the observation of a decrease in the Hall mobility of the charge carriers mentioned above (see Figure 6b). It should be noted that N doping introduces a significant number of defects and causes changes

in the structural and electronic properties of graphitic materials.[19,42] As a general observation, a high density of defects, resulting from high N doping in the form of pyridinic-N and pyrrolic-N, leads to a decrease in the charge carrier mobility as a consequence of the large number of π electrons localized around the defect sites. Therefore, in this work, the changes in the electron and hole mobilities in relation to the N doping are well correlated with the density of defects in N-doped nanocrystalline graphene films.

3. CONCLUSIONS

In summary, we reported an attempt of the direct growth of N-doped nanocrystalline graphene films via a low-temperature cold-wall plasma-assisted CVD method in a C_6H_6/NH$_3$/Ar system. It was found that fully covered N-doped nanocrystalline graphene films can be effectively grown on a pretreated Ni film at low-temperature regimes as low as 100 °C. Unlike existing N-doped graphene, the as-grown films here are composed of highly defective N-containing polycrystalline nanodomains. The influences of the NH$_3$/Ar ratio and plasma power on the N doping were systematically investigated, wherein the synergetic effects are key to the fine-tuning graphene growth with pyridinic-N or pyrrolic-N at low temperatures. At a low NH$_3$/Ar ratio or low plasma power, the resulting graphene growth favored more pyridinic-N than pyrrolic-N. Conversely, at a high NH$_3$/Ar ratio or high plasma power, pyrrolic-N-dominated graphene growth, which is mostly associated with defects at the edges, presented substantial N doping up to values of 11.28 at.%. In addition, the N-doped nanocrystalline graphene films dominated by pyridinic-N and pyrrolic-N exhibit n-type semiconductor behavior with a strong asymmetry in electron−hole conduction under ambient air conditions. Our findings here provide significant progress toward the establishment of a high-throughput plasma-assisted CVD method and also contribute to designing novel materials with a practical strategy of heteroatom nitrogen doping at low temperatures for future transparent nanodevices.

4. EXPERIMENTAL SECTION

4.1. Growth of N-Doped Nanocrystalline Graphene Films. A 150 nm thick polycrystalline Ni film (99.99%, Kurt J. Lesker), as a catalyst, was deposited on the SiO$_2$/Si (100) substrate via a radio frequency magnetron sputtering system (Edwards TF-600) at a base pressure of 0.2 Pa and room temperature. The growth of N-doped nanocrystalline graphene films was performed in a cold-wall plasma-assisted CVD system (Oxford Instruments, PlasmalabSystem 100), as illustrated in Figure 7a,b. Prior to the growth process, the samples were annealed at 700 °C by direct Joule heating under continuous 100 sccm hydrogen H$_2$ (99.999%) and 100 sccm argon Ar (99.99999%) at a pressure of 200 Pa for 60 min. H$_2$ gas was introduced into the chamber to further remove the remaining carbon and oxygen impurities. The samples were then cooled down to the desired growth temperature (400, 300, 200, and 100 °C, respectively) in an Ar atmosphere. To confirm the contaminant-free samples before and after the annealing step, the samples were characterized and verified by Raman measurements (see Figure S1). For the growth process, after reaching the desired temperature by direct Joule heating, the growth of N-doped nanocrystalline graphene films was carried out in a mixture ratio of 1:1:8 (C_6H_6/NH$_3$/Ar) at the

same pressure with a minimum of 10 W plasma power for 1 h. Noted that the uniform plasma field generated on the surface can cover up to a diameter of ~230 mm with a vertical distance of ~50 mm. For this system, the liquid benzene (C_6H_6) source (≥99.9%, Sigma-Aldrich) that was kept in a bubbler at room temperature was transported into the reaction chamber with a 20 sccm Ar flow rate as the carrier gas, while purified Ar with 160 sccm flow rate (99.99999%) and NH$_3$ (99.999%) with 20 sccm flow rate introduced during the growth process were transported separately. In this work, the influences of the NH$_3$/Ar flow rate ratio (0.125, 0.1875, and 0.25) and radio frequency (RF) power (10, 20, and 50 W) on the growth of nanocrystalline graphene films were further investigated at 100 °C. Finally, the samples were transferred to a load lock and rapidly cooled to room temperature in vacuum (<0.133 Pa). The overall growth process in this work is shown in Figure 7c,d.

4.2. Sample Characterization. Prior to the characterization of N-doped nanocrystalline graphene films, the as-grown samples were transferred onto SiO$_2$/Si (100), a quartz substrate, and a lacey carbon-coated Cu grid by a wet chemical transfer method.[29] The transfer was initiated with spin coating of 100 nm thick poly(methyl methacrylate) (PMMA) on the as-grown samples (1 cm × 1 cm), followed by curing the samples at 80 °C on a hot plate for 5 min and immersing the whole samples in 0.1 M ferric chloride (FeCl$_3$) for a sufficiently long time to remove the Ni film. The resulting N-doped nanocrystalline graphene films with PMMA in the form of a transparent film were transferred in the deionized water to clean the Ni residues and the FeCl$_3$ etching agents. Then, the transparent film was transferred to the target substrate, where the remaining PMMA was removed in acetone. The morphology and structural properties of the transferred samples were characterized by a field-emission scanning electron microscopy (FESEM) system (JEOL, JSM-7500F) operating at an accelerating voltage of 2.0 kV and a high-resolution transmission electron microscopy (HR-TEM) system (JEOL, JEM-2010) operating at an accelerating voltage of 200 kV. To investigate their elemental composition and N doping configuration in the graphene film, X-ray photoelectron spectroscopy (XPS) measurements were carried out using an X-ray photoelectron spectrometer system (Scanning XPS Microprobe, PHI Quantera II). The XPS system was operated under the conditions of a maximum photon electron of 600 eV with 0.1 eV kinetic energy steps for a narrow scan. For the structural analysis of N-doped nanocrystalline graphene films, Raman spectra measurements were performed at room temperature with laser excitation at 514 nm using a Raman spectroscopy system (WITec α 300). For the electrical measurements, a Hall-effect measurement system (Ecopia, HMS-5300) was used to characterize the transferred N-doped nanocrystalline graphene films on the SiO$_2$/Si substrate in ambient air at 300 K. In the same conditions, the back-gated field-effect transistor (FET), utilizing the N-doped nanocrystalline graphene films, was also characterized using a source meter unit (SMU) system (Keithley 236).

■ ASSOCIATED CONTENT

Ⓢ Supporting Information

The Supporting Information is available free of charge at https://pubs.acs.org/doi/10.1021/acsomega.1c01520.

Raman spectra analysis of the samples before and after the annealing process (Figure S1), energy-dispersive X-ray spectroscopy (EDS) elemental mapping analysis (Figure S2), X-ray diffraction (XRD) pattern of the N-doped nanocrystalline graphene films on the polycrystalline Ni film (Figure S3), and Raman mapping measurements of N-doped nanocrystalline graphene films (Figure S4) (PDF)

■ AUTHOR INFORMATION

Corresponding Authors

Muhammad Aniq Shazni Mohammad Haniff − *Institute of Microengineering and Nanoelectronics, Universiti Kebangsaan Malaysia, 43600 Bangi, Malaysia;* ◉ orcid.org/0000-0003-3980-3460; Email: aniqshazni@ukm.edu.my

Abdul Manaf Hashim − *Advanced Devices and Material Engineering Research Lab, Department of Electronic Systems Engineering, Malaysia-Japan International Institute of Technology, Universiti Teknologi Malaysia, 51400 Kuala Lumpur, Malaysia;* Email: abdmanaf@utm.my

Authors

Nur Hamizah Zainal Ariffin − *Advanced Devices and Material Engineering Research Lab, Department of Electronic Systems Engineering, Malaysia-Japan International Institute of Technology, Universiti Teknologi Malaysia, 51400 Kuala Lumpur, Malaysia; Advanced Devices Lab, MIMOS Berhad, 57000 Kuala Lumpur, Malaysia*

Mohd Ismahadi Syono − *Advanced Devices Lab, MIMOS Berhad, 57000 Kuala Lumpur, Malaysia*

Mohd Ambri Mohamed − *Institute of Microengineering and Nanoelectronics, Universiti Kebangsaan Malaysia, 43600 Bangi, Malaysia*

Azrul Azlan Hamzah − *Institute of Microengineering and Nanoelectronics, Universiti Kebangsaan Malaysia, 43600 Bangi, Malaysia*

Complete contact information is available at:
https://pubs.acs.org/10.1021/acsomega.1c01520

Author Contributions

N.H.Z.A. and M.A.S.M.H. contributed equally to this work. N.H.Z.A. and M.A.S.M.H. directed and wrote the main manuscript text. The design, growth, and characterization of N-doped graphene were conducted by N.H.Z.A. M.A.S.M.H., M.I.S., M.A.M., A.A.H., and A.M.H. provided support in the monitoring, verification of the results, and revision of the manuscript. All authors approved the manuscript.

Notes

The authors declare no competing financial interest.

■ REFERENCES

(1) Geim, A. K.; Novoselov, K. S. The rise of graphene. *Nat. Mater.* **2007**, *6*, 183−191.

(2) Schwierz, F. Graphene transistors. *Nat. Nanotechnol.* **2010**, *5*, 487−496.

(3) Becerril, H. A.; Mao, J.; Liu, Z.; Stoltenberg, R. M.; Bao, Z.; Chen, Y. Evaluation of solution-processed reduced graphene oxide films as transparent conductors. *ACS Nano* **2008**, *2*, 463−470.

(4) Kim, K. S.; Zhao, Y.; Jang, H.; Lee, S. Y.; Kim, J. M.; Kim, K. S.; Ahn, J. H.; Kim, P.; Choi, J. Y.; Hong, B. H. Large-scale pattern growth of graphene films for stretchable transparent electrodes. *Nature* **2009**, *457*, 706−710.

(5) Abdullah, M. F.; Hashim, A. M. Improved coverage of rGO film on Si inverted pyramidal microstructures for enhancing the photovoltaic of rGO/Si heterojunction solar cell. *Mater. Sci. Semicond. Process.* **2019**, *96*, 137−144.

(6) Mohammad Haniff, M. A. S.; Ariffin, N. H. Z.; Hafiz, S. M.; Ooi, P. C.; Syono, M. I.; Hashim, A. M. Wafer-scale fabrication of nitrogen-doped reduced graphene oxide with enhanced quaternary-N for high-performance photodetection. *ACS Appl. Mater. Interfaces* **2019**, *11*, 4625−4636.

(7) Feng, X.; He, Z.; Zhu, W.; Zhao, M.; Liu, Z.; Yang, S.; Tang, S.; Guo, Q.; Jin, Z.; Chen, D.; Ding, G.; Wang, G. Perovskite quantum dots integrated with vertically aligned graphene toward ambipolar multifunctional photodetectors. *J. Mater. Chem. C* **2021**, *9*, 609−619.

(8) Zhao, Y.; Feng, X.; Zhao, M.; Zeng, X.; Liu, Z.; Yang, S.; Tang, S.; Chen, D.; Wang, G.; Ding, G. High-performance near-infrared photodetectors based on C_3N quantum dots integrated with single-crystal graphene. *J. Mater. Chem. C* **2021**, *9*, 1333−1338.

(9) Shao, Y.; Wang, J.; Wu, H.; Liu, J.; Aksay, I. A.; Lin, Y. Graphene based electrochemical sensors and biosensors: A review. *Electroanalysis* **2010**, *22*, 1027−1036.

(10) Zhao, M.; Zhu, W.; Feng, X.; Yang, S.; Liu, Z.; Tang, S.; Chen, D.; Guo, Q.; Wang, G.; Ding, G. Role of interface 2D graphene in high performance 3D graphene/germanium Schottky junction humidity sensors. *J. Mater. Chem. C* **2020**, *8*, 14196−14202.

(11) Li, J.; Liu, Z.; Guo, Q.; Yang, S.; Xu, A.; Wang, Z.; Wang, G.; Wang, Y.; Chen, D.; Ding, G. Controllable growth of vertically oriented graphene for high sensitivity gas detection. *J. Mater. Chem. C* **2019**, *7*, 5995−6003.

(12) Novoselov, K. S.; Geim, A. K.; Morozov, S. V.; Jiang, D.; Zhang, Y.; Dubonos, S. V.; Grigorieva, I. V.; Firsov, A. A. Electric field effect in atomically thin carbon films. *Science* **2004**, *306*, 666−669.

(13) Berger, C.; Song, Z.; Li, X.; Wu, X.; Brown, N.; Naud, C.; Mayou, D.; Li, T.; Hass, J.; Marchenkov, A. N.; Conrad, E. H.; First, P. N.; de Heer, W. A. Electronic confinement and coherence in patterned epitaxial graphene. *Science* **2006**, *312*, 1191−1196.

(14) Guo, B.; Fang, L.; Zhang, B.; Gong, J. R. Graphene doping: A review. *Insci. J.* **2011**, *1*, 80−89.

(15) Lee, H.; Paeng, K.; Kim, I. S. A review of doping modulation in graphene. *Synth. Met.* **2018**, *244*, 36−47.

(16) Geng, D.; Yang, S.; Zhang, Y.; Yang, J.; Liu, J.; Li, R.; Sham, T. K.; Sun, X.; Ye, S.; Knights, S. Nitrogen doping effects on the structure of graphene. *Appl. Surf. Sci.* **2011**, *257*, 9193−9198.

(17) Wang, H.; Maiyalagan, T.; Wang, X. Review on recent progress in nitrogen-doped graphene: Synthesis, characterization, and its potential applications. *ACS Catal.* **2012**, *2*, 781−794.

(18) Matter, P. H.; Zhang, L.; Ozkan, U. S. The role of nanostructure in nitrogen-containing carbon catalyst for the oxygen reduction reaction. *J. Catal.* **2006**, *239*, 83−96.

(19) Wei, D.; Liu, Y.; Wang, Y.; Zhang, H.; Huang, L.; Yu, G. Synthesis of N-doped graphene by chemical vapor deposition and its electrical properties. *Nano Lett.* **2009**, *9*, 1752−1758.

(20) Luo, Z.; Lim, S.; Tian, Z.; Shang, J.; Lai, L.; MacDonald, B.; Fu, C.; Shen, Z.; Yu, T.; Lin, J. Pyridinic N doped graphene: Synthesis, electronic structure, and electrocatalytic property. *J. Mater. Chem.* **2011**, *21*, 8038−8044.

(21) Sui, Y.; Zhu, B.; Zhang, H.; Shu, H.; Chen, Z.; Zhang, Y.; Zhang, Y.; Wang, B.; Tang, C.; Xie, X.; Yu, G.; Jin, Z.; Liu, X.

Temperature-dependent nitrogen configuration of N-doped graphene by chemical vapor deposition. *Carbon* **2015**, *81*, 814−820.

(22) Jin, Z.; Yao, J.; Kittrell, C.; Tour, J. M. Large-scale growth and characterizations of nitrogen-doped monolayer graphene sheets. *ACS Nano* **2011**, *5*, 4112−4117.

(23) Zabet-Khosousi, A.; Zhao, L.; Pálová, L.; Hybertsen, M. S.; Reichman, D. R.; Pasupathy, A. N.; Flynn, G. W. Segregation of sublattice domains in nitrogen-doped graphene. *J. Am. Chem. Soc.* **2014**, *136*, 1391−1397.

(24) Weatherup, R. S.; Bayer, B. C.; Blume, R.; Ducati, C.; Baehtz, C.; Schlogl, R.; Hofmann, S. In situ characterization of alloy catalyst for low temperature graphene growth. *Nano Lett.* **2011**, *11*, 4154−4160.

(25) Mohammad Haniff, M. A. S.; Ariffin, N. H. Z.; Ooi, P. C.; Razip Wee, M. F. M. R.; Mohamed, M. A.; Hamzah, A. A.; Syono, M. I.; Hashim, A. M. Practical route for the low-temperature growth of large-area bilayer graphene on polycrystalline nickel by cold-wall chemical vapor deposition. *ACS Omega* **2021**, *6*, 12143−12154.

(26) Terasawa, T.; Saiki, K. Synthesis of nitrogen-doped graphene by plasma-enhanced chemical vapor deposition. *Jpn. J. Appl. Phys.* **2012**, *51*, No. 055101.

(27) Wang, C.; Zhao, Y.; He, L.; Ng, T. W.; Hong, G.; Wu, Q. H.; Gao, F.; Lee, C. S.; Zhang, W. In situ nitrogen doped graphene grown from polydimethylsiloxane by plasma enhanced chemical vapor deposition. *Nanoscale* **2013**, *5*, 600−605.

(28) Wei, D.; Peng, L.; Li, M.; Mao, H.; Niu, T.; Han, C.; Chen, W.; Wee, A. T. S. Low temperature critical growth of high quality nitrogen doped graphene on dielectrics by plasma-enhanced chemical vapor deposition. *ACS Nano* **2015**, *9*, 164−171.

(29) Boas, C. R. S. V.; Focassio, B.; Marinho, E., Jr.; Larrude, D. G.; Salvadori, M. C.; Leao, C. R.; dos Santos, D. J. Characterization of nitrogen doped graphene bilayers synthesized by fast, low temperature microwave plasma-enhanced chemical vapour deposition. *Sci. Rep.* **2019**, *9*, No. 13715.

(30) Zhang, J.; Li, J.; Wang, Z.; Wang, X.; Feng, W.; Zheng, W.; Cao, W.; Hu, P. Low temperature growth of large- area heteroatom-doped graphene film. *Chem. Mater.* **2014**, *26*, 2460−2466.

(31) Xue, Y.; Wu, B.; Jiang, L.; Guo, L.; Huang, I.; Chen, J.; Tan, J.; Geng, D.; Luo, B.; Hu, W.; Yu, G.; Liu, Y. Low temperature growth of highly nitrogen-doped single crystal graphene arrays by chemical vapor deposition continuous graphene films from benzene by chemical vapor deposition. *J. Am. Chem. Soc.* **2012**, *134*, 11060−11063.

(32) Son, M.; Chee, S.-S.; Kim, S.-Y.; Lee, W.; Kim, Y. H.; Oh, B.-Y.; Hwang, J. Y.; Lee, B. H.; Ham, M.-H. High-quality nitrogen-doped graphene films synthesized from pyridine via two-step chemical vapor deposition. *Carbon* **2020**, *159*, 579−585.

(33) Jang, J.; Son, M.; Chung, S.; Kim, K.; Cho, C.; Lee, B. H.; Ham, M.-H. Low-temperature-grown continuous graphene films from benzene by chemical vapor deposition at ambient pressure. *Sci. Rep.* **2015**, *5*, No. 17955.

(34) Li, X. S.; Cai, W. W.; An, J. H.; Kim, S.; Nah, K.; Yang, D. X.; Piner, R.; Velamakanni, A.; Jung, I.; Tutuc, E.; Banerjee, S. K.; Colombo, L.; Ruoff, R. S. Large-area synthesis of high-quality and uniform graphene films on copper foils. *Science* **2009**, *324*, 1312−1314.

(35) McNerny, D. Q.; Viswanath, B.; Copic, D.; Laye, F. R.; Prohoda, C.; Brieland-Shoultz, A. C.; Polsen, E. S.; Dee, N. T.; Veerasamy, V. S.; Hart, A. J. Direct fabrication of graphene on SiO$_2$ enabled by thin film stress engineering. *Sci. Rep.* **2015**, *4*, No. 5049.

(36) Nair, R. R.; Blake, P.; Grigorenko, A. N.; Novoselov, K. S.; Booth, T. J.; Stauber, T.; Peres, N. M. R.; Geim, A. K. Fine structure constant defines visual transparency of graphene. *Science* **2008**, *320*, 1308.

(37) Capasso, A.; Dikonimos, T.; Sarto, F.; Tamburrano, A.; De Bellis, G.; Sarto, M. S.; Faggio, G.; Malara, A.; Messina, G.; Lisi, N. Nitrogen-doped graphene films from chemical vapor deposition of pyridine: Influence of process parameters on the electrical and optical properties. *Beilstein J. Nanotechnol.* **2015**, *6*, 2028−2038.

(38) Sun, J.; Chen, Y.; Cai, X.; Ma, B.; Chen, Z.; Priydarshi, M. K.; Chen, K.; Gao, T.; Song, X.; Ji, Q.; Guo, X.; Zou, D.; Zhang, Y.; Lui, Z. Direct low-temperature synthesis of graphene on various glasses by plasma-enhanced chemical vapor deposition for versatile, cost-effective electrodes. *Nano Res.* **2015**, *8*, 3496−3504.

(39) Weber, N.-E.; Binder, A.; Kettner, M.; Hirth, S.; Weitz, R. T.; Tomović, Ž. Metal-free synthesis of nanocrystalline graphene on insulating substrates by carbon dioxide-assisted chemical vapor deposition. *Carbon* **2017**, *112*, 201−207.

(40) Muñoz, R.; Munuera, C.; Martínez, J. I.; Azpeitia, J.; Gómez-Aleixandre, C.; García-Hernández, M. Low temperature metal free growth of graphene on insulating substrates by plasma assisted chemical vapor deposition. *2D Mater.* **2017**, *4*, No. 015009.

(41) Haniff, M. A. S. M.; Hafiz, S. M.; Huang, N. M.; Rahmah, S. A.; Wahid, K. A. A.; Syono, M. I.; Azid, I. A. Piezoresistive effect in plasma-doping of graphene sheet for high-performance flexible pressure sensing application. *ACS Appl. Mater. Interfaces* **2017**, *9*, 15192−15201.

(42) Lu, Y.-F.; Lo, S.-T.; Lin, J.-C.; Zhang, W.; Lu, J.-Y.; Liu, F.-H.; Tseng, C.-H.; Lee, Y.-H.; Liang, C.-T.; Li, L.-J. Nitrogen-doped graphene sheets grown by chemical vapor deposition: Synthesis and influence of nitrogen impurities on carrier transport. *ACS Nano* **2013**, *7*, 6522−6532.

(43) Koós, A. A.; Murdock, A. T.; Nemes-Icnze, P.; Nicholls, R. J.; Pollard, A. J.; Spencer, S. J.; Shard, A. G.; Roy, D.; Biró, L. P.; Grobert, N. Effects of temperature and ammonia flow rate on the chemical vapour deposition growth of nitrogen-doped graphene. *Phys. Chem. Chem. Phys.* **2014**, *16*, 19446−19452.

(44) Zhang, J.; Zhao, C.; Liu, N.; Zhang, H.; Liu, J.; Fu, Y. Q.; Guo, B.; Wang, Z.; Lei, S.; Hu, P. Tunable electronic properties of graphene through controlling bonding configurations of doped nitrogen atoms. *Sci. Rep.* **2016**, *6*, No. 28330.

(45) Wang, L.; Yi, Y.; Zhao, Y.; Zhang, R.; Zhang, J.; Guo, H. NH$_3$ decomposition for H$_2$ generation: Effects of cheap metals and supports on plasma-catalyst synergy. *ACS Catal.* **2015**, *5*, 4167−4174.

(46) Wei, D.; Lu, Y.; Han, C.; Niu, T.; Chen, W.; Wee, A. T. S. Critical crystal growth of graphene on dielectric substrates at low temperature for electronic devices. *Angew. Chem., Int. Ed.* **2013**, *52*, 14121−14126.

(47) Gan, X.; Zhou, H.; Zhu, B.; Yu, X.; Jia, Y.; Sun, B.; Zhang, M.; Huang, X.; Liu, J.; Luo, T. A simple method to synthesize graphene at 633 k by dechlorination of hexachlorobenzene on cu foils. *Carbon* **2012**, *50*, 306−310.

(48) Zheng, S.; Zhong, G.; Wu, X.; D'Arsiè, L.; Robertson, J. Metal-catalyst-free growth of graphene on insulating substrates by ammonia-assisted microwave plasma-enhanced chemical vapor deposition. *RSC Adv.* **2017**, *7*, 33185−33193.

(49) Zhang, C.; Fu, L.; Liu, N.; Liu, M.; Wang, Y.; Liu, Z. Synthesis of nitrogen-doped graphene using embedded carbon and nitrogen sources. *Adv. Mater.* **2011**, *23*, 1020−1024.

(50) Venezuela, P.; Lazzeri, M.; Mauri, F. Theory of double-resonant raman spectra in graphene: Intensity and line shape of defect-induced and two-phonon bands. *Phys. Rev. B* **2011**, *84*, No. 035433.

(51) Casiraghi, C.; Hartschuh, A.; Qian, H.; Piscanec, S.; Georgi, C.; Fasoli, A.; Novoselov, K. S.; Basko, D. M.; Ferrari, A. Raman spectroscopy of graphene edges. *Nano Lett.* **2009**, *9*, 1433−1441.

(52) Cuong, N. K.; Tahara, M.; Yamauchi, N.; Sone, T. Diamond-like carbon films deposited on polymers by plasma-enhanced chemical vapor deposition. *Surf. Coat. Technol.* **2003**, *174−175*, 1024−1028.

(53) Das, A.; Pisana, S.; Chakraborty, B.; Picsanec, S.; Saha, S. K.; Waghmare, U. V.; Novoselov, K. S.; Krishnamurthy, H. R.; Geim, A. K.; Ferrari, A. C.; Sood, A. K. Monitoring dopants by raman scattering in an electrochemically top-gated graphene transistor. *Nat. Nanotechnol.* **2008**, *3*, 210−215.

(54) Deng, D.; Pan, X.; Yu, L.; Cui, Y.; Jiang, Y.; Qi, J.; Li, W.-X.; Fu, Q.; Ma, X.; Xue, Q.; Sun, G.; Bao, X. Toward N-doped graphene via solvothermal synthesis. *Chem. Mater.* **2011**, *23*, 1188−1193.

(55) Cançado, L. G.; Jorio, A.; Martins Ferreira, E. H.; Stavale, F.; Achete, C. A.; Capaz, R. B.; Moutinho, M. V. O.; Lambardo, A.;

Kulmala, T. S.; Ferrari, A. C. Quantifying defects in graphene via raman spectroscopy at different excitation energies. *Nano Lett.* **2011**, *11*, 3190−3196.

(56) Jin, Z.; Yao, J.; Kittrel, C.; Tour, J. M. Large-scale growth and characterizations of nitrogen-doped monolayer graphene sheets. *ACS Nano* **2011**, *5*, 4112.

(57) Tuinstra, F.; Koenig, J. L. Raman spectrum of graphite. *J. Chem. Phys.* **1970**, *53*, 1126.

(58) He, B.; Ren, Z.; Qi, C.; Yan, S.; Wang, Z. Synthesis of nitrogen-doped monolayer graphene with high transparent and n-type electrical properties. *J. Mater. Chem. C* **2015**, *3*, 6172−6177.

(59) Hofer, C.; Skákalová, V.; Görlich, T.; Tripathi, M.; Mittelberger, A.; Mangler, C.; Monazam, M. R. A.; Susi, T.; Kotakoski, J.; Meyer, J. C. Direct imaging of light-element impurities in graphene reveals triple-coordinated oxygen. *Nat. Commun.* **2019**, *10*, No. 4570.

(60) Yuk, J. M.; Park, J.; Ercius, P.; Kim, K.; Hellebusch, D. J.; Crommie, M. F.; Lee, J. Y.; Zettl, A.; Alivisatos, A. P. High-resolution EM of colloidal nanocrystal growth using graphene liquid cells. *Science* **2012**, *336*, 61−64.

(61) Meyer, J. C.; Kurasch, S.; Park, H. J.; Skalalova, V.; Künzel, D.; Groß, A.; Chuvilin, A.; Algara-Siller, G.; Roth, S.; Iwasaki, T.; Starke, U.; Smet, J. H.; Kaiser, U. Experimental analysis of charge redistribution due to chemical bonding by high-resolution transmission electron microscopy. *Nat. Mater.* **2011**, *10*, 209−215.

(62) Snow, E. S.; Novak, J. P.; Campbell, P. M.; Park, D. Random networks of carbon nanotubes as an electronic material. *Appl. Phys. Lett.* **2003**, *82*, 2145.